

# Particle beam microstructure reconstruction and coincidence discrimination in PET monitoring for hadron therapy

E Kostara<sup>1,2</sup>, G Sportelli<sup>1,3,\*</sup>, N Belcari<sup>1,3</sup>, N Camarlinghi<sup>1,3</sup>, P Cerello<sup>5</sup>, A Del Guerra<sup>3</sup>, V Ferrero<sup>4,5</sup>, E Fiorina<sup>5</sup>, G Giraudo<sup>5</sup>, M Morrocchi<sup>1</sup>, F Pennazio<sup>5</sup>, M Pullia<sup>6</sup>, A Rivetti<sup>5</sup>, M D Rolo<sup>5</sup>, V Rosso<sup>1,3</sup>, R Wheadon<sup>5</sup>, M G Bisogni<sup>1,3</sup>

<sup>1</sup> Istituto Nazionale di Fisica Nucleare (INFN), Pisa, Italy

<sup>2</sup> Department of Physical Sciences, Earth and Environment, University of Siena, Siena, Italy

<sup>3</sup> Department of Physics, University of Pisa, Pisa, Italy

<sup>4</sup> Department of Physics, University of Torino, Torino, Italy

<sup>5</sup> Istituto Nazionale di Fisica Nucleare (INFN), Torino, Italy

<sup>6</sup> Fondazione CNAO, Strada Campeggi 53, 27100 Pavia, Italy

\* Corresponding author

E-mail: giancarlo.sportelli@unipi.it

**Abstract.** Positron emission tomography is one of the most mature techniques for monitoring the particles range in hadron therapy, aiming to reduce treatment uncertainties and therefore the extent of safety margins in the treatment plan.

In-beam PET monitoring has been already performed using inter-spill and post-irradiation data, i.e., while the particle beam is off or paused. The full beam acquisition procedure is commonly discarded because the particle spills abruptly increase the random coincidence rates and therefore the image noise. This is because random coincidences cannot be separated by annihilation photons originating from radioactive decays and cannot be corrected with standard random coincidence techniques due to the time correlation of the beam-induced background with the ion beam microstructure.

The aim of this paper is to provide a new method to recover in-spill data to improve the images obtained with full-beam PET acquisitions. This is done by estimating the temporal microstructure of the beam and thus selecting input PET events that are less likely to be random ones. The PET detector we used was the one developed within the INSIDE project and tested at the CNAO synchrotron-based facility. The data were taken on a PMMA phantom irradiated with 72 MeV proton pencil beams. The obtained results confirm the possibility of improving the acquired PET data without any external signal coming from the synchrotron or ad-hoc detectors.

*Keywords:* in-beam PET monitoring, random correction techniques, fast Fourier transform

## 1. Introduction

Cancer therapy with protons or heavy ions has the potential of delivering highly conformal dose distributions to the tumor while sparing the surrounding tissue. This happens because charged particles have a finite depth penetration range characterized by the Bragg peak at the end. At present, positron emission tomography (PET) is the most exploited technique in clinics for *in vivo* and non-invasive monitoring of radiation treatments [Enghardt et al., 1999, Enghardt et al., 2004, Zhu et al., 2011, Combs et al., 2012, Del Guerra et al., 2016, Parodi, 2016]. During proton treatments, nuclear reactions between the projectiles and the target nuclei of the traversed tissue produce positrons emitters. PET scanners can detect the emitted positron-electron annihilation photons in the patient during and after the treatment. Studies showed the potential of PET for a millimeter accuracy in both range monitoring and lateral verification of the dose delivery in proton irradiation [Parodi et al., 2007, Parodi et al., 2008, Knopf et al., 2008, Attanasi et al., 2011, Ferrero et al., 2018, Fiorina et al., 2018, Pennazio et al., 2018].

The PET data acquisition can be performed in either one of the following three alternatives: during the particle irradiation with the patient on the treatment bed (in-beam), inside the treatment room but moving the patient to an independent PET machine (in-room) and outside the treatment room on a separate facility (off-line) [Shakirin et al., 2011]. In synchrotron-based facilities, beam irradiations are structured in the form of spills and pauses of lengths both in the order of seconds. These two intervals together make the so-called extraction-acceleration cycle. When acquiring in-beam, we can be further distinguish acquisitions that are carried out during spills (in-spill), during the beam pauses (inter-spill), and after the end of the irradiation. We refer to the union of in-spill, inter-spill and post-irradiation datasets as full-beam acquisitions [Sportelli et al., 2013].

One of the main benefits of in-beam monitoring with respect to off-line and in-room monitoring, is that the first is less affected by artefacts due to patient motion and biological washout [Helmbrecht et al., 2013, Parodi, 2015]. However, in-spill data are corrupted by the prompt noise generated by the beam, inter-spill data are generally few because of the short acquisition time and post-irradiation data is limited by practical constraints on room occupancy and patient immobilization. Moreover, post-irradiation count rates acquired by in-beam PET detectors can be lower than those available to full ring PET systems, due to the more constrained detector geometry. This situation motivates the research for new acquisition techniques and PET detector technologies in order to improve the quantity and quality of in-beam data.

The strong noise that is present during the spills is due to the increased random coincidence rate induced by the high prompt radiation background [Parodi et al., 2005]. This background might originate from  $\gamma$ -rays following nuclear reactions not related to  $\beta^+$  decay [Enghardt et al., 2004] or from pair productions and neutrons. Such random events cannot be separated from the usable decays of  $\beta^+$  emitters [Enghardt et al., 1999, Parodi et al., 2001]. Moreover, they cannot be corrected with standard random

coincidence correction techniques because of the time-correlation of the beam-induced background with the ion beam microstructure [Parodi et al., 2005].

Until now, the only way to identify and filter out coincidence events that occur during the bunch, i.e., in the most noisy phase interval of the periodic extraction-acceleration cycle, was by recording an external signal coming from the accelerator or using an additional particle detector [Crespo et al., 2005].

The objective of this work is to implement a processing algorithm that allows to perform such identification and filtering on the basis of the time distribution of the acquired events [Sportelli et al., 2018]. An approach based on the data processing has been already presented in [Piliero et al., 2016], where a time-resolved spectroscopic analysis of the events in a microbunch has been performed, assuming that the particle bunch enters the target at the time of the first prompt gamma detected for each burst of events.

Our technique operates in a way similar to what has been already done in [Crespo et al., 2005], but without using any additional device between the beam and the PET data or any external synchronisation with the accelerator. It also uses the same principle of [Piliero et al., 2016] that short bursts of prompt events are acquired in correspondence of particle extractions.

The expected advantages are three: 1) the in-beam PET system installation does not require any major intervention on the beam line; 2) it operates directly on the acquired data, thus avoiding any systematic phase error due to the spread of the transit time of input particles from the trigger to the PET detectors; 3) it uses time information averaged over intervals that span multiple extraction-acceleration cycles, thus increasing the precision of the phase detection scheme.

This paper is organised as follows. In the first part the PET detector, the experimental set-up and the data processing are described. In particular, we present a processing algorithm that uses in-spill data in order to calculate the period of the beam microstructure. Also, a method for filtering the in-spill data is described. In the second part, the results for the algorithm are presented along with the resulting images for in-spill and inter-spill data.

## 2. Materials and methods

### 2.1. PET detector

The PET detector is composed of two modules of  $5.12 \times 5.12$  cm<sup>2</sup> detection area each, placed at 50 cm one from the other. Each module consists of an array of 16x16 Lutetium Fine Silicate (LFS) crystals with  $3.2 \times 3.2 \times 20$  mm<sup>3</sup> size. The crystals are coupled one to one to an array of  $16 \times 16$  Hamamatsu S12642-1616 silicon photomultipliers (SiPMs).

The read-out electronics of each PET module consist of four 64-channels front-end (FE) ASICs, designed for time-of-flight PET (TOFPET) [Rolo et al., 2013]. Each ASIC is hosted in a custom FE board and supports an input event rate up to

100 kHz per channel. For each event, the FE board provides the released energy and the arrival time (timestamp). The FE board is connected to a Xilinx Virtex-6 FPGA ML605 evaluation board [Xilinx, 2017]. The system clock of the FPGA is set at 120 MHz. Two sensors are mounted on the FE boards to monitor the temperature of the read-out system, which is kept constant at 36°C using fans.

The PET detector is a small prototype of the PET scanner developed within the INSIDE (INnovative SolutIons for DosimEtry in hadrontherapy) project for the in-beam monitoring of head and neck hadron therapy treatments [Bisogni et al., 2017, Fiorina et al., 2016, Marafini et al., 2015, Pennazio et al., 2015]. The INSIDE PET system is made of two planar panels with  $10 \times 25$  cm<sup>2</sup> detection area. Each panel is composed of 10 detection modules arranged in a  $2 \times 5$  array. A more detailed description of the PET module can be found in [Bisogni et al., 2017].

### 2.2. Experimental set-up

The PET detector was tested at the Centro Nazionale di Adroterapia Oncologica (CNAO) in Pavia, Italy. Figure 1a shows the experimental set-up into the treatment room at CNAO [Piliero et al., 2016]. A polymethyl methacrylate (PMMA) phantom was irradiated with proton pencil beams that hit the center of the phantom's entrance surface.

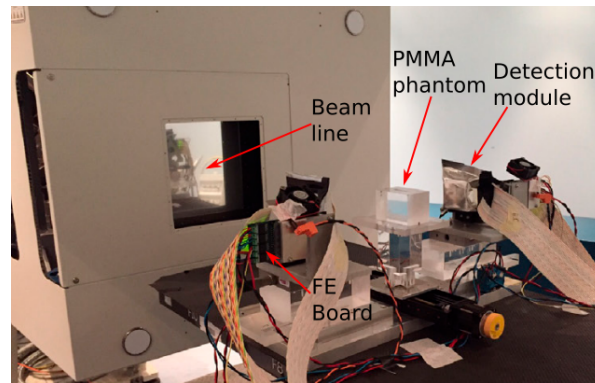
The PMMA phantom with a size of  $4.9 \times 4.9 \times 7$  cm<sup>3</sup> was placed between the two PET detector modules with the long side along the beam direction. The entrance surface of the phantoms was located 1 cm inside the detectors field of view (FOV). The distance between the central axis of the PMMA and the detection modules was set to 25 cm. The layout of the experimental set-up is presented in Figure 1b, along with the beam direction and the spatial reference system.

### 2.3. Beam characteristics

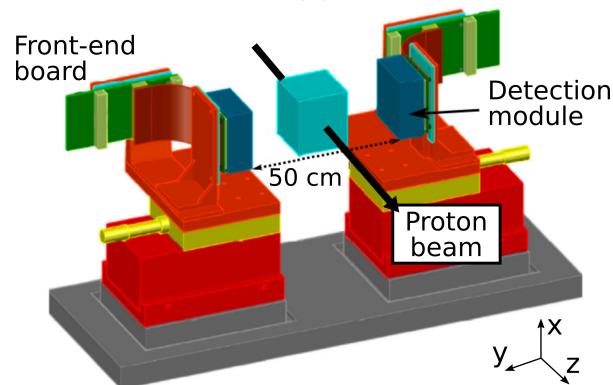
The CNAO synchrotron beam time structure is a sequence of 1 s beam-on (in-spill) followed by 4 s beam-off (inter-spill). The beam intensity was set to  $2 \times 10^9$  protons per spill. The protons energy was 72 MeV, which corresponds to 40 mm Bragg peak depth in water. The total number of protons was  $2 \times 10^{11}$ , delivered in 98 spills for a total time of 490 s.

The temporal microstructure of the extracted beam of the CNAO synchrotron shows a strong correlation with the accelerator radio frequency (RF) due to its characteristic slow extraction scheme. Each spill is characterized by bunches of tens or hundreds of nanoseconds, depending on the extraction energy, equally spaced in time following the RF period of the accelerator. The events acquired by the PET system have similar a temporal microstructure that is related to the bunches length and the RF period.

The RF structure in the extracted beam is due to the fact that the RF cavity is running during the slow extraction, in order to perform the so called empty bucket



(a)



(b)

**Figure 1:** (a) Experimental set-up in the treatment room at CNAO. (b) Layout (not to scale) of the experimental set-up. Reprinted with permission from [Piliero et al., 2016].

channelling method [Cappi and Steinbach, 1981].

The RF structure of the CNAO accelerator includes a frequency sweep for spill stabilisation. The sweep is periodic, with a triangular trend and a period of  $100 \mu\text{s}$ . The amplitude of the frequency sweep was  $\Delta f = 15 \text{ kHz}$  peak-to-peak with an initial frequency  $f_{\text{RF}} = 1.43715 \text{ MHz}$ , which is specific to the 72 MeV beam energy.

#### 2.4. Data processing

The acquired data are saved in a single list mode file and include in-spill, inter-spill and post-irradiation events. The TOFPET ASIC provides the timestamp and the released energy of each event. The released energy is obtained in the analog FE stage with the time over threshold (ToT) method. Two threshold levels are set. When the pulse crosses the low and high thresholds on the rising edge, timestamp  $t_0$  is recorded and  $t_1$  is used by the control logic for hit validation. On the falling edge, when the pulse crosses back the high threshold, a second timestamp  $t_2$  is recorded. The pulse duration is measured as the difference between the timestamps  $t_0$  and  $t_2$ , and it is a monotonic function of the energy, i.e.,  $\text{energy} = f(\text{ToT}) = f(t_2 - t_0)$ . The higher  $t_1$  threshold is used to validate the events, rejecting the dark counts of the SiPMs, while the low  $t_0$  threshold allows

to minimize the walk error for timing discrimination. More details about the working principle of the TOFPET ASIC can be found in [Rolo et al., 2013].

*2.4.1. Preliminary data filtering.* The distribution of the single events rate as a function of time reproduces the pulsed time structure of the beam with beam-on 1 s and beam-off 4 s, as shown in Figure 2. This distribution is used to preprocess the data and identify the start and stop timestamps of each spill by means of a threshold on the single count rate. These timestamps are then used to separate in-spill from inter-spill data.

In the beam-on intervals, many of the events acquired by the detector during the spill are due to prompt events (gammas and neutrons) deriving from nuclear de-excitation/evaporation, which constitute the background noise, and from gammas deriving from the annihilation of positrons emitted after  $\beta^+$  decays of radioisotopes produced by nuclear fragmentations, which are our signal.

In the beam-off intervals, the acquired events (inter-spill data) are only those deriving from the annihilation of the positrons emitted after  $\beta^+$  decays of the radioisotopes produced by nuclear fragmentations. In these intervals, the background is minimum and it is due to random coincidences.

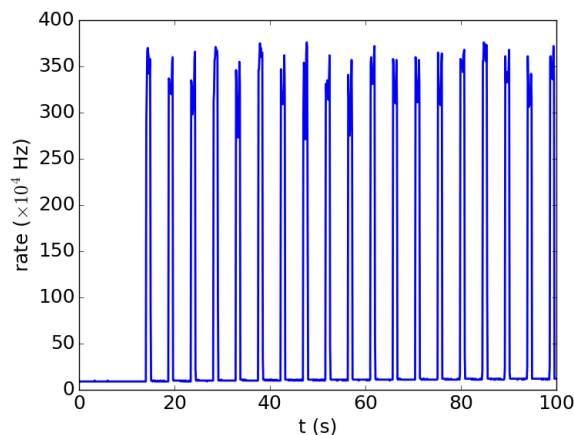


**Figure 2:** Single event rate distribution as a function of time used to separate in-spill from inter-spill data. Reprinted with permission from [Piliro et al., 2016].

*2.4.2. Algorithm for the calculation of the period of the beam microstructure and the phase of each acquired event.* The beam microstructure is expected to change from spill to spill. Hence, the acquired data are analyzed separately per spill.

For each spill, a fine-grained event rate (FGER) is calculated, i.e., the rate of events that fall in very short time intervals. The interval length used in this study is 1 ns. At the dose rates of interest, the statistical accuracy of the FGER is very low, because in bins of 1 ns it is unlikely to have even only one event. Still, the FGER retains accurately the temporal properties that we need in order to retrieve the period of the accelerator RF. The aim is to find the main component of the Fourier representation of the FGER,

which is expected to be close to the RF. This is being done by applying a Fast Fourier Transform (FFT) directly to the FGER. The peak found with the FFT at the null frequency would correspond to the average event rate on the whole spill interval. The second one in the MHz range is expected to correspond to the RF. We refer to it as frequency  $f_0$ . This frequency can be found automatically by searching for the highest peak in the MHz range. The first estimation of the RF period is thus  $T_0=1/f_0$ . Based on this first estimation, we can assign a phase value  $\phi_i$  with respect to  $T_0$  to each event  $i$ :

$$\phi_i = t_i \bmod T_0, \quad (1)$$

where  $t_i$  is the timestamp of event  $i$  and  $\bmod$  is the modulo operator. Knowing the event phases, it is possible to calculate the histogram of such phases. The normalised form of such histogram will represent the probability of an event occurring in each sub-interval of the RF period, in a way that resembles the microbunch intensity as already published in simulation [Parodi et al., 2005]. We refer to this probability distribution as “virtual microbunch”. The shape of the virtual microbunch depends strongly on the accuracy of the period estimation. In fact, the drift error on phases estimation due to period inaccuracies accumulates over time and limits the capability of analyzing long acquisition intervals altogether. We can mitigate this effect by iteratively searching the period  $T_j$  around  $T_0$  that maximizes the peak to valley ratio of the virtual microbunch. This has been done on experimental data by applying (1) for different values of  $T_j$  in the  $[T_{(j-1)} \pm t_r]$  range, where  $t_r$  is reduced at each iteration  $j$ , until it provides the best estimation of the microbunch period ( $T_s$ ). The iterative search is stopped when the improvement in peak to valley ratio is below an arbitrary threshold. A flow diagram of the iterative method is shown in Figure 3.

A phase offset is also added to center the peak of the probability distribution with respect to the period, so that the phase  $\phi_i$  becomes:

$$\phi_i = t_i \bmod T_s + \phi_b, \quad (2)$$

where  $t_i$  is the timestamp of event  $i$ ,  $T_s$  is the best estimation of the microbunch period and  $\phi_b$  is the phase offset.

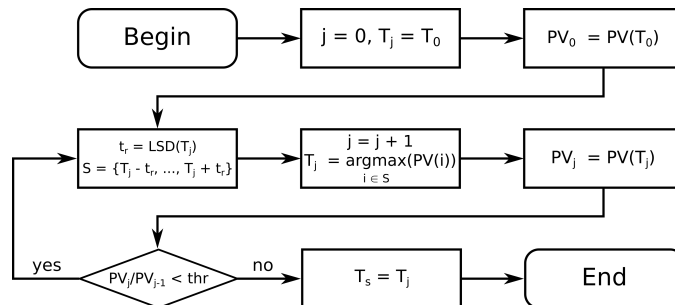


**Figure 3:** Flow diagram of the iterative procedure used to estimate the period of the microbunch.  $LSD(T_j)$  is the least significant digit of  $T_j$ .

*2.4.3. Filtering the in-spill data.* We filter the random events using the  $\phi_i$  information as calculated above. In particular, we want to remove all the events that fall in correspondence to the passage of the microbunch through the target, i.e., all those events whose phase falls within a predetermined window around the peak found in the virtual microbunch and calculated over the estimated period  $T_s$ . In order to define a phase rejection window, a Gaussian fit is applied to the peak of the virtual microbunch. The parameters of the Gaussian fit, mean  $\mu$  and standard deviation  $\sigma$ , are then saved for every spill. The best results were obtained by setting a phase rejection window of  $\mu \pm 2\sigma$  over the period  $T_s$ . Thus, coincidence events that occur within the rejection window are removed. Events outside this window are considered as occurring between microbunches and thus are selected for reconstruction. These events are referred to as in-spill inter-bunches data.

*2.4.4. Image reconstruction and activity profile.* An energy window is defined to discriminate all the events that are close to the 511 keV annihilation peak. Due to the non-linear energy response of TOFPET ASIC, this discrimination is done by defining an allowed ToT range on post-irradiation data as in [Bisogni et al., 2017].

We use a maximum-likelihood expectation-maximization (ML-EM) algorithm to reconstruct the image. Five iterations are executed in 1 s on a 2.10 GHz Intel Core i7-3612QM CPU. More details on the reconstruction algorithm are available in [Camarlinghi et al., 2014]. The reconstructed FOV is  $51.2 \times 51.2 \times 51.2 \text{ mm}^3$  with  $1.6 \text{ mm}^3$  voxels.

An initial analysis is carried out using inter-spill and in-spill data. One-dimensional activity profiles are traced along the beam direction on the reconstructed image. To reduce statistical fluctuations, the activity profile is obtained by averaging the 4 central slices parallel to the PET detectors, starting from the center of the  $x$  axis.

### 3. Results and discussion

#### 3.1. Calculation of the period of the beam microstructure

A typical FGER is presented in Figure 4. The detected events are sparse in time, thus the number of the events in each bin is generally small. This is visible in Figure 4 where the maximum number of observed counts is three, and several bins contain no events at all.

The FFT calculated on the FGER of Figure 4 is plotted in Figure 5. In Figure 5a, the first peak is the average event rate on the whole spill interval. The second one is  $f_0 = 1.4384 \text{ MHz}$ , which is compatible with the RF of the accelerator at CNAO. Consequently, the first period estimation is  $T_0 = 1/f_0 = 695.2 \text{ ns}$ . In Figure 5b, two other smaller peaks are observed. The first one at 10 kHz is supposed to correspond to the period of the RF sweep for spill stabilization. The second one at 20 kHz is supposed to be related to the frequency of the voltage reference of the magnets power supplies.

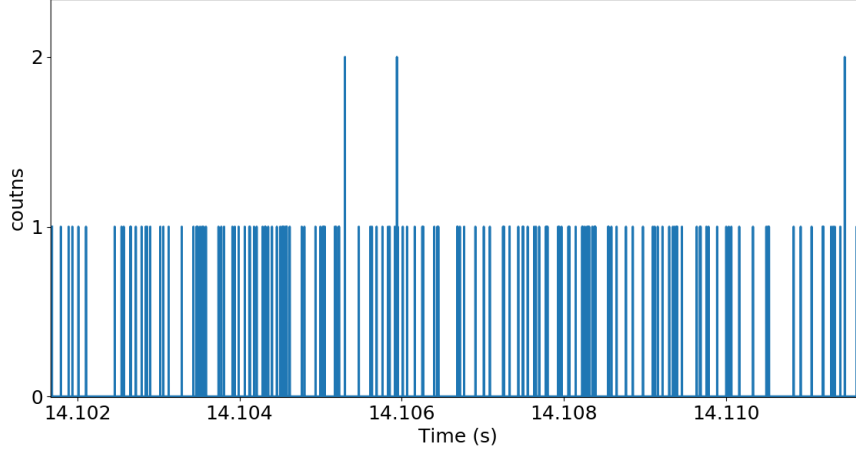


**Figure 4:** FGER calculated over a subset of the data related to a single spill.

However, the influence from power supplies has not been verified yet.

This first estimation  $T_0$  is used as starting value for the calculation of the virtual microbunch. The algorithm searches around  $T_0$  in the range  $[T_0 \pm 200 \text{ ps}]$ , using a step of 0.5 ps, looking for the period that maximizes the peak of the histogram. Figure 6a shows the microbunch obtained using  $T_0 = 695.2 \text{ ns}$ . Figure 6d shows the best estimation of the period  $T_s = 695.2165 \text{ ns}$ . The optimization of the period leads to the minimization of the FWHM of the virtual microbunch distribution. Figures 6b and 6c show the representation of the microbunch in two intermediate estimations (second and third) of the period, i.e.,  $T_1 = 695.2085 \text{ ns}$  and  $T_2 = 695.2160 \text{ ns}$ .

Note that the plots in Figure 6 represent the number of events supposed to occur

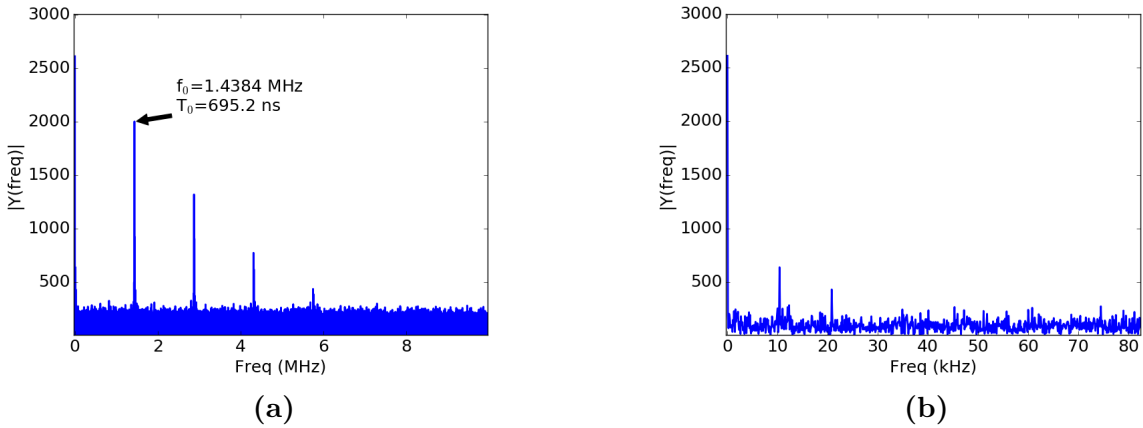


**Figure 5:** FFT calculated on the FGER of a single spill. **(a)** View in the MHz range. The second highest peak is at frequency  $f_0=1.4384 \text{ MHz}$ . The corresponding period is  $T_0=1/f_0=695.2 \text{ ns}$ . **(b)** Zoom on the two peaks at 10 kHz and 20 kHz, which are specific to the CNAO extraction scheme and power supplies operation.

at a given time offset with respect to the acceleration/extraction cycle for different period estimations. Therefore, the value on the y-axis is not an event rate. It should be intended instead as the probability of having an event at a given time offset with respect to the estimated period.

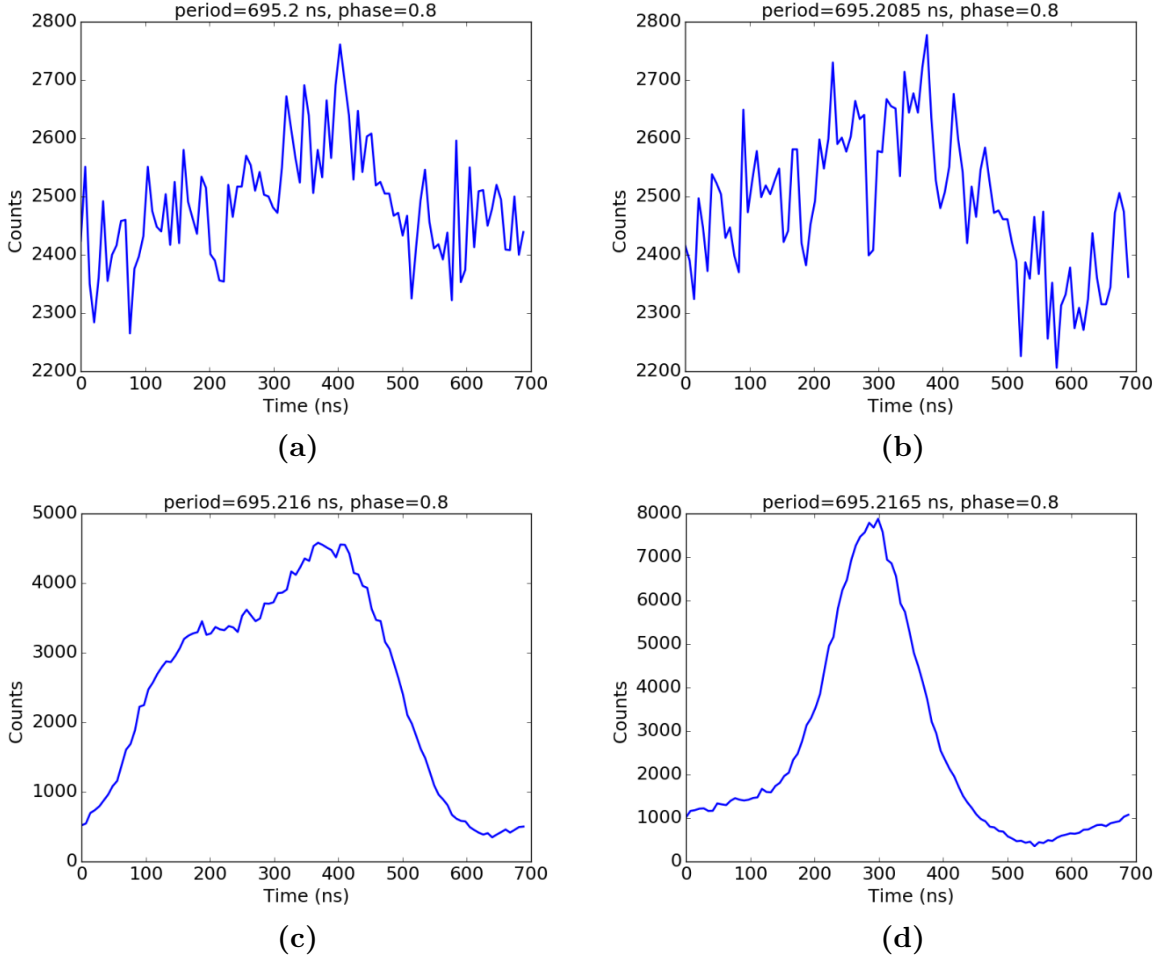


**Figure 6:** Representation of the virtual microbunch as it is iteratively reconstructed: (a) using the first period estimation  $T_0 = 695.2$  ns as it is derived from the FFT; (b) using the second estimation  $T_1 = 695.2058$  ns; (c) using the third estimation  $T_2 = 695.216$  ns; (d) using the best estimation  $T_s = 695.2165$  ns.

### 3.2. Width of the virtual microbunch

Figure 7 shows a Gaussian fit ( $\mu=339$  ns,  $\sigma=75$  ns) applied to the peak of the virtual microbunch. The window around the peak of the spill is chosen to be equal to  $\mu \pm 2\sigma$ . By discarding the data inside this window, more than 65% of the total coincidences are removed.

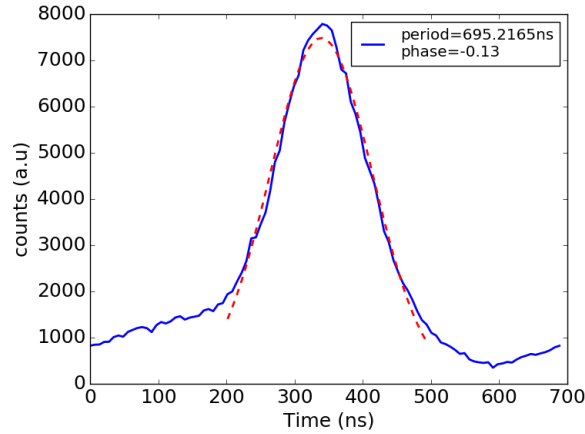


**Figure 7:** Gaussian fit of the peak of the virtual microbunch.

### 3.3. 3D spatial distributions of coincident events

Figures 8a and 8b present the reconstructed images of inter-spill and in-spill data, respectively. Only the central slice in the x-z plane of the FOV is shown (the reference frame is presented in Figure 1b). The beam enters from the left side. The image obtained from in-spill data is noisier than the one obtained from inter-spill data. In particular, it can be noticed in Figure 8b: a higher intensity at the left extremity of the field of view, before the entrance surface of the PMMA phantom, i.e., outside the irradiated volume; a background intensity in general higher than in the reference image in Figure 8a.

The reconstructed image obtained using the in-spill inter-bunches data is shown in Figure 8c. The figure shows that the entrance artefact and the image noise are significantly reduced.

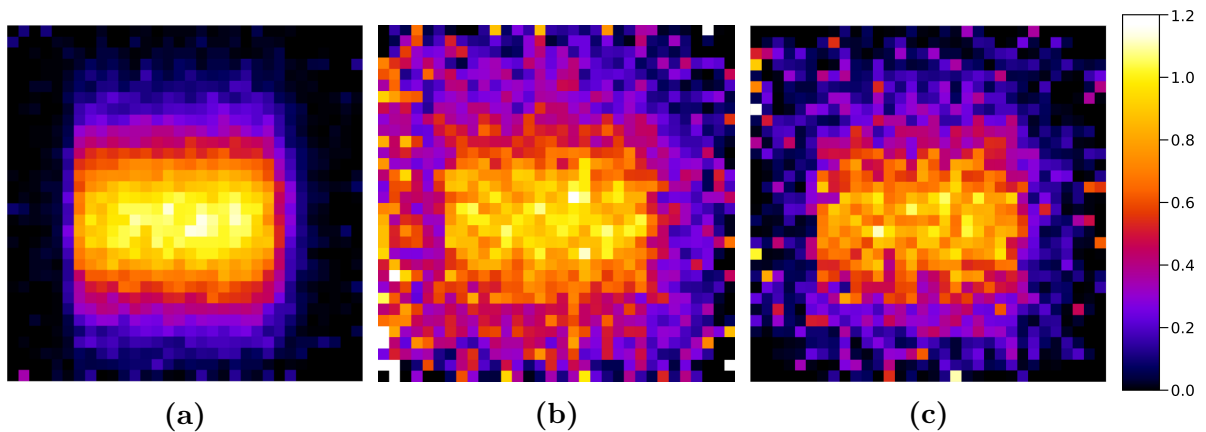


**Figure 8:** Image reconstruction of (a) inter-spill coincidence events; (b) in-spill coincidence events; (c) in-spill inter-bunches (after filtering) coincidence events. The figures show the activity in the x-z plane at the center of the FOV. The beam direction is from left to right. In (c), image artefacts and the noisy background are significantly reduced with respect to (b).

### 3.4. 1D activity profiles of positron emitters

The activity profiles calculated over Figures 8a, 8b and 8c are shown in Figure 9. In the in-spill case, the artefacts from the radiation background are visible as higher activities at the entrance surface of the phantom and at the distal end of the activated volume. The number of coincidence events before the entrance surface of the phantom decreases significantly when the filter is applied.

The tail artefact at the end of the activity range of the in-spill inter-bunches data is not influenced by the filter.

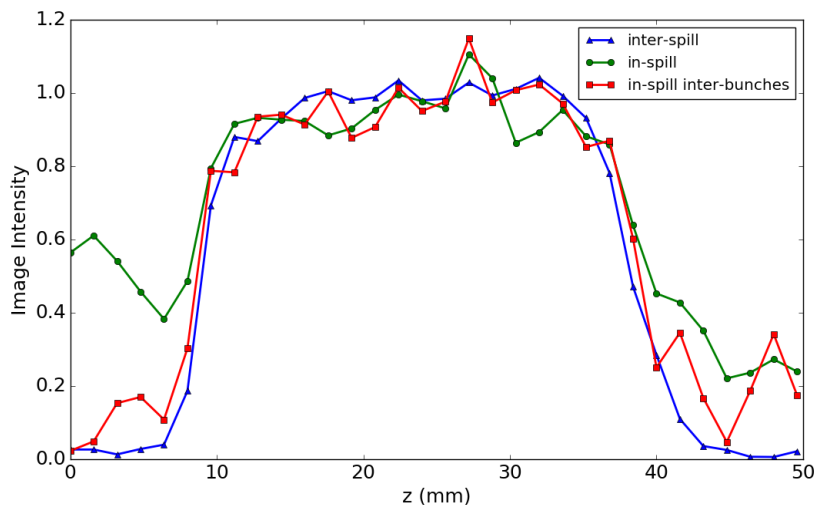


**Figure 9:** Activity profiles calculated over Figure 8 for inter-spill, in-spill, in-spill inter-bunches (i.e., after phase filtering) coincidence events.

## 4. Discussion

The reconstructed images for inter-spill and in-spill data show that the in-spill distribution is noisier than the inter-spill one, in part due to the limited statistics during the spills which occupy a fraction of 20% of the whole acquisition time. Furthermore, additional noise comes from the high radiation background and random coincidence rates that are due to the beam-induced prompt events, i.e., those events that do not originate from nuclear decays. The reconstructed images present also severe artefacts close to the entrance and the exit of the PMMA phantom. This is particularly evident when analysing the activity distribution on PMMA phantoms such as the one in Figure 8 (b) and the relative profile in Figure 9 (in-spill).

In an effort to find a way to eliminate these artefacts by reducing the image corrupting events, we have made a spectral analysis applying a FFT to the time of arrival of any single event acquired by the PET system.

We have shown that it is possible to find the main particle extraction frequency in the spectrum by applying a FFT to the FGER. We have also observed in the spectrum

additional features that might be related to the power supply and ripple reduction techniques that are specific to the CNAO accelerator. However, the influence of the power supply needs to be verified. The precision achievable with the sole FFT was not sufficient to reliably divide the time frame of the acquisition into acceleration/extraction cycles, so as to discriminate the events by their probability of occurring during an extraction, and thus by their probability of being a spurious event.

It was possible to overcome this limitation by refining the RF value obtained with the FFT with an iterative numerical optimization. The main assumption behind the iterative optimization is that the most likely RF is the one that arranges the event phases in the most compact virtual microbunch. Applying this technique we have actually found a peak of event occurrences in a limited phase range (approximately 75 ns  $\sigma$  over a period of 695 ns).

After discarding the coincidence events that occur in the virtual microbunch, more than 65% of the coincidence events in-spill were removed. At the same time, we observed a sensible reduction of the background artefacts at the entrance side. Before the entrance, annihilations are improbable and thus we should not expect any significant reconstructed activity. At the distal edge, positrons emitted by short-lived isotopes with relatively higher energy end-points [Dendooven et al., 2015], and therefore longer positron ranges, can annihilate inside the phantom, farther from the isotope itself. On the one hand, such annihilations are not related to the beam time structure and hence cannot be suppressed by the filter, on the other hand they decay too quickly to be acquired off-beam or inter-spills. For these reasons, the in-spill and in-spill inter-bunches profiles at the distal edge are less different in comparison with the proximal edge.

This analysis is based on the timestamps of single events which are normally discarded in conventional PET imaging. Therefore, it is possible only if the data acquisition system is able to record all the single event timestamps. In this way an off-line processing would allow to find the in-spill inter-bunches. However, acquiring all the timestamps for a large PET system could prove to be unfeasible, due to the very high bandwidth required to sustain the input event rates.

## 5. Conclusions

We have shown that the temporal information contained in every single event acquired by PET can be exploited to identify the fine temporal structure of the particles entering the target. This fine structure can in turn be used to distinguish spurious events from those actually coming from  $\beta^+$  nuclear decays, as it was already done before with an external phase trigger coming from either a hardware interface to the accelerator or a fast particle detector in the beam path. The potential advantages of this technique are the lower hardware complexity due to the lack of external synchronisation hardware, the higher flexibility due to the all-digital implementation and better filtering efficiency because of the possibility of using averaged timing information along several acceleration/extraction cycles.

The new method has been tested on a PET detector that can acquire all the single events during the irradiation of PMMA phantoms with 72 MeV protons at CNAO. The results show that it is possible to remove part of the artifacts induced by in-spill noise in the reconstructed images. Conventional PET data acquisition systems might be unable to allow this type of analysis, because they don't normally have enough acquisition speed to collect all the single events; therefore, it is under study an alternative on-chip data filtering technique based on Field Programmable Gate Array (FPGA) [Kostara, 2017] which allows to perform real-time filtering on the data before its storage for reconstruction.

## Acknowledgements

This work has been mainly supported by the Italian Ministry of University and Research (MIUR) under the program PRIN 2010/2011 INSIDE project 2010P98A75. The authors are also very grateful to CNAO personnel, particularly to Mario Ciocca, Marco Donetti and Sandro Rossi for their kind collaboration in the data acquisition and the discussion of results.

## References

- [Attanasi et al., 2011] Attanasi, F., Knopf, A., Parodi, K., Paganetti, H., Bortfeld, T., Rosso, V., and Del Guerra, A. (2011). Extension and validation of an analytical model for in vivo PET verification of proton therapy: A phantom and clinical study. *Physics in medicine and biology*, 56(16):5079.
- [Bisogni et al., 2017] Bisogni, M. G., Attili, A., Battistoni, G., Belcari, N., Cerello, P., Coli, S., Del Guerra, A., Ferrari, A., Ferrero, V., Fiorina, E., et al. (2017). INSIDE in-beam positron emission tomography system for particle range monitoring in hadrontherapy. *Journal of Medical Imaging*, 4(1):011005–011005.
- [Camarlinghi et al., 2014] Camarlinghi, N., Sportelli, G., Battistoni, G., Belcari, N., Cecchetti, M., Cirrone, G., Cuttone, G., Ferretti, S., Kraan, A., Retico, A., et al. (2014). An in-beam PET system for monitoring ion-beam therapy: test on phantoms using clinical 62 MeV protons. *Journal of Instrumentation*, 9(04):C04005.
- [Cappi and Steinbach, 1981] Cappi, R. and Steinbach, C. (1981). Low Frequency Duty Factor Improvement for the CERN PS Slow Extraction Using RF Phase Displacement Techniques. *IEEE Transactions on Nuclear Science*, 28(3):2806–2808.
- [Combs et al., 2012] Combs, S. E., Bauer, J., Unholtz, D., Kurz, C., Welzel, T., Habermehl, D., Haberer, T., Debus, J., and Parodi, K. (2012). Monitoring of patients treated with particle therapy using positron-emission-tomography (PET): the MIRANDA study. *BMC cancer*, 12(1):133.
- [Crespo et al., 2005] Crespo, P., Barthel, T., Fraiss-Kolbl, H., Griesmayer, E., Heidel, K., Parodi, K., Pawelke, J., and Enghardt, W. (2005). Suppression of random coincidences during in-beam PET measurements at ion beam radiotherapy facilities. *IEEE transactions on nuclear science*, 52(4):980–987.
- [Del Guerra et al., 2016] Del Guerra, A., Belcari, N., and Bisogni, M. (2016). Positron emission tomography: its 65 years. *Riv. Nuovo Cimento*, 39:155.
- [Dendooven et al., 2015] Dendooven, P., Buitenhuis, H. J. T., Diblen, F., Heeres, P. N., Biegun, A. K., Fiedler, F., Goethem, M.-J. v., Graaf, E. R. v. d., and Brandenburg, S. (2015). Short-lived positron emitters in beam-on PET imaging during proton therapy. *Physics in Medicine & Biology*, 60(23):8923.

- [Enghardt et al., 2004] Enghardt, W., Crespo, P., Fiedler, F., Hinz, R., Parodi, K., Pawelke, J., and Pönisch, F. (2004). Charged hadron tumour therapy monitoring by means of PET. *Nuclear Instruments and Methods in Physics Research Section A: Accelerators, Spectrometers, Detectors and Associated Equipment*, 525(1):284–288.
- [Enghardt et al., 1999] Enghardt, W., Debus, J., Haberer, T., Hasch, B. G., Hinz, R., Jäkel, O., Krämer, M., Lauckner, K., and Pawelke, J. (1999). The application of PET to quality assurance of heavy-ion tumor therapy. *Strahlentherapie und Onkologie*, 175(2):33–36.
- [Ferrero et al., 2018] Ferrero, V., Fiorina, E., Morrocchi, M., Pennazio, F., Baroni, G., Battistoni, G., Belcari, N., Camarlinghi, N., Ciocca, M., Guerra, A. D., Donetti, M., Giordanengo, S., Giraud, G., Patera, V., Peroni, C., Rivetti, A., Rolo, M. D. d. R., Rossi, S., Rosso, V., Sportelli, G., Tampellini, S., Valvo, F., Wheadon, R., Cerello, P., and Bisogni, M. G. (2018). Online proton therapy monitoring: clinical test of a Silicon-photodetector-based in-beam PET. *Scientific Reports*, 8(1):4100.
- [Fiorina et al., 2016] Fiorina, E., collaboration, I., et al. (2016). An integrated system for the online monitoring of particle therapy treatment accuracy. *Nuclear Instruments and Methods in Physics Research Section A: Accelerators, Spectrometers, Detectors and Associated Equipment*, 824:198–201.
- [Fiorina et al., 2018] Fiorina, E., Ferrero, V., Pennazio, F., Baroni, G., Battistoni, G., Belcari, N., Cerello, P., Camarlinghi, N., Ciocca, M., Del Guerra, A., Donetti, M., Ferrari, A., Giordanengo, S., Giraud, G., Mairani, A., Morrocchi, M., Peroni, C., Rivetti, A., Da Rocha Rolo, M. D., Rossi, S., Rosso, V., Sala, P., Sportelli, G., Tampellini, S., Valvo, F., Wheadon, R., and Bisogni, M. G. (2018). Monte Carlo simulation tool for online treatment monitoring in hadrontherapy with in-beam PET: A patient study. *Physica Medica*, 51:71–80.
- [Helmbrecht et al., 2013] Helmbrecht, S., Enghardt, W., Parodi, K., Diding, B., Debus, J., Kunath, D., Priegnitz, M., and Fiedler, F. (2013). Analysis of metabolic washout of positron emitters produced during carbon ion head and neck radiotherapy. *Medical Physics*, 40(9):091918.
- [Knopf et al., 2008] Knopf, A., Parodi, K., Paganetti, H., Cascio, E., Bonab, A., and Bortfeld, T. (2008). Quantitative assessment of the physical potential of proton beam range verification with PET/CT. *Physics in medicine and biology*, 53(15):4137.
- [Kostara, 2017] Kostara, E. (2017). *Full-beam PET monitoring in hadron therapy and related coincidence logic*. PhD thesis, Department of Earth and Environmental Sciences - University of Siena.
- [Marafini et al., 2015] Marafini, M., Frallicciardi, P., Faccini, R., Morone, C., Voena, C., Patera, V., Piersanti, L., Sciubba, A., Attili, A., Coli, S., et al. (2015). The INSIDE project: INnovative SolutIons for in-beam DosimEtry in hadrontherapy. *Acta Physica Polonica, A*, 127(5).
- [Parodi, 2015] Parodi, K. (2015). Vision 20/20: Positron emission tomography in radiation therapy planning, delivery, and monitoring. *Medical physics*, 42(12):7153–7168.
- [Parodi, 2016] Parodi, K. (2016). On-and off-line monitoring of ion beam treatment. *Nuclear Instruments and Methods in Physics Research Section A: Accelerators, Spectrometers, Detectors and Associated Equipment*, 809:113–119.
- [Parodi et al., 2008] Parodi, K., Bortfeld, T., and Haberer, T. (2008). Comparison between in-beam and offline positron emission tomography imaging of proton and carbon ion therapeutic irradiation at synchrotron-and cyclotron-based facilities. *International Journal of Radiation Oncology\* Biology\* Physics*, 71(3):945–956.
- [Parodi et al., 2005] Parodi, K., Crespo, P., Eickhoff, H., Haberer, T., Pawelke, J., Schardt, D., and Enghardt, W. (2005). Random coincidences during in-beam PET measurements at microbunched therapeutic ion beams. *Nuclear Instruments and Methods in Physics Research Section A: Accelerators, Spectrometers, Detectors and Associated Equipment*, 545(1):446–458.
- [Parodi et al., 2001] Parodi, K., Enghardt, W., and Haberer, T. (2001). In-beam PET measurements of  $\beta^+$  radioactivity induced by proton beams. *Physics in medicine and biology*, 47(1):21.
- [Parodi et al., 2007] Parodi, K., Paganetti, H., Cascio, E., Flanz, J. B., Bonab, A. A., Alpert, N. M.,

- Lohmann, K., and Bortfeld, T. (2007). PET/CT imaging for treatment verification after proton therapy: a study with plastic phantoms and metallic implants. *Medical physics*, 34(2):419–435.
- [Pennazio et al., 2015] Pennazio, F., Attili, A., Cerello, P., Coli, S., Giraudo, G., Rivetti, A., Wheadon, R., Fiorina, E., Peroni, C., Battistoni, G., et al. (2015). A study of monitoring performances with the INSIDE system. *Acta Physica Polonica, A.*, 127(5).
- [Pennazio et al., 2018] Pennazio, F., Battistoni, G., Bisogni, M. G., Camarlinghi, N., Alfredo Ferrari, Ferrero, V., Fiorina, E., Morrocchi, M., Sala, P., Sportelli, G., Richard Wheadon, and Cerello, P. (2018). Carbon ions beam therapy monitoring with the INSIDE in-beam PET. *Physics in Medicine & Biology*, 63(14):145018.
- [Piliro et al., 2016] Piliro, M., Pennazio, F., Bisogni, M., Camarlinghi, N., Cerello, P., Del Guerra, A., Ferrero, V., Fiorina, E., Giraudo, G., Morrocchi, M., et al. (2016). Full-beam performances of a PET detector with synchrotron therapeutic proton beams. *Physics in medicine and biology*, 61(23):N650.
- [Rolo et al., 2013] Rolo, M., Bugalho, R., Gonçalves, F., Mazza, G., Rivetti, A., Silva, J., Silva, R., and Varela, J. (2013). TOFPET ASIC for PET applications. *Journal of Instrumentation*, 8(02):C02050.
- [Shakirin et al., 2011] Shakirin, G., Braess, H., Fiedler, F., Kunath, D., Laube, K., Parodi, K., Priegnitz, M., and Enghardt, W. (2011). Implementation and workflow for PET monitoring of therapeutic ion irradiation: a comparison of in-beam, in-room, and off-line techniques. *Physics in medicine and biology*, 56(5):1281.
- [Sportelli et al., 2013] Sportelli, G., Belcari, N., Camarlinghi, N., Cirrone, G., Cuttone, G., Ferretti, S., Kraan, A., Ortuño, J., Romano, F., Santos, A., et al. (2013). First full-beam PET acquisitions in proton therapy with a modular dual-head dedicated system. *Physics in medicine and biology*, 59(1):43.
- [Sportelli et al., 2018] Sportelli, G., Bisogni, M., Kostara, E., Morrocchi, M., and Camarlinghi, N. (2018). Metodo ed apparato per l’acquisizione dati per tomografia ad emissione di positroni in adroterapia a fascio acceso. Italian Patent App. n. 102018000000867.
- [Xilinx, 2017] Xilinx (2017). UG535 ML605 reference design, user guide, ver 1.0. [https://www.xilinx.com/support/documentation/boards\\_and\\_kits/ug535.pdf](https://www.xilinx.com/support/documentation/boards_and_kits/ug535.pdf). [visited on 21-March-2017].
- [Zhu et al., 2011] Zhu, X., España, S., Daartz, J., Liebsch, N., Ouyang, J., Paganetti, H., Bortfeld, T. R., and El Fakhri, G. (2011). Monitoring proton radiation therapy with in-room PET imaging. *Physics in medicine and biology*, 56(13):4041.